Nat. Hazards Earth Syst. Sci., 10, 1051–1059, 2010
www.nat-hazards-earth-syst-sci.net/10/1051/2010/
doi:10.5194/nhess-10-1051-2010

Natural Hazards and Earth System Sciences

An expression for the water-sediment moving layer in unsteady flows valid for open channels and embankments

A. M. Berta and G. Bianco

Dipartimento di Idraulica Trasposti ed Infrastrutture Civili, Politecnico di Torino, Torino, Italy

Received: 5 October 2009 – Revised: 5 February 2010 – Accepted: 23 February 2010 – Published: 28 May 2010

Abstract. During the floods, the effects of sediment transport in river beds are particulary significant and can be studied through the evolution of the water-sediment layer which moves in the lower part of a flow, named "moving layer". Moving layer variations along rivers lead to depositions and erosions and are typically unsteady, but are often tackled with expressions developed for steady (equilibrium) conditions. In this paper, we develop an expression for the moving layer in unsteady conditions and calibrate it with experimental data. During laboratory tests, we have in fact reproduced a rapidly changing unsteady flow by the erosion of a granular steep slope. Results have shown a clear tendency of the moving layer, for fixed discharges, toward equilibrium conditions. Knowing the equilibrium achievement has presented many difficulties, being influenced by the choice of the equilibrium expression and moreover by the estimation of the parameters involved (for example friction angle). Since we used only data relevant to hyper-concentrated mono-dimensional flows for the calibration – occurring for slope gradients in the range 0.03–0.20 – our model can be applied both on open channels and on embankments/dams, providing that the flows can be modelled as mono-dimensional, and that slopes and applied shear stress levels fall within the considered ranges.

1 Introduction

Sediment transport effects are particulary significant during the floods and their study is important for a better understanding of hydrodynamical and morphological processes. A useful indicator of the sediment discharge is the depth of the water-sediment layer which moves in the lower part of a stream, named "moving layer" or "bed load layer" (Egashira and Ashida, 1992). If related to the flow depth (measured from the granular layer that is not in motion), the moving layer is commonly used to distinguish the different kinds of flow (ordinary flow, hyper-concentrated flow). For example, ordinary flows present a ratio far less than unity between the width of the moving layer and the depth of the water-sediment flow. Hyper-concentrated flows are instead characterised by a moving layer comparable to flow depth, and so not negligible. A correct evaluation of the moving layer is particularly important when the sediment transport is intense, because mistakes may have many consequences on the water level estimation.

Transport processes in alluvial channels are usually unsteady and produce spatial and temporal changes of river morphology that can be related to the continuous variation of moving layer thickness. Unfortunately, there are only few works regarding the unsteady non-uniform sediment transport, and unsteady flows are usually treated with expressions that have been developed for a uniform flow condition (Papa et al., 2004; Egashira et al., 2001; Franzi, 2001; Correira et al., 1992; Takahashi, 1991) that is often described as the "equilibrium condition" (Seminara, 1998). This approach is incorrect for purely unsteady flows, for which the immediate achievement of transport capacity, which actually occurs in equilibrium conditions, is not ensured (Armanini and Di Silvio, 1988). The immediate achievement of transport capacity can be admitted, usually for granular materials, when time dependent effects are negligible. This approximation is not reliable for strictly unsteady flow (with a strong dependence on time) and with little erosion length available. In fact, in some of their tests carried out with constant liquid discharge, Di Silvio and Gregoretti (1997) doubted that equilibrium conditions were effectively reached as a consequence of a too short erodible flume.

In this paper, we propose an expression for a reliable estimation of the moving layer during unsteady conditions. This novel formulation is calibrated with data acquired in laboratory tests. Since the failure of earthen levees or embankments represents a reference application for unsteady transport (Fraccarollo and Capart, 2002; Cao et al., 2004; Wang

Correspondence to: A. M. Berta
(anna.berta@polito.it)

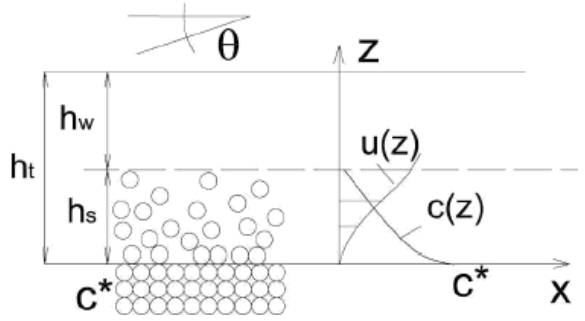

Fig. 1. Sketch of the moving layer depth h_s of a flow over an erodible bed. Profiles for velocity $u(z)$ and sediment concentration $c(z)$ (Egashira and Ashida, 1992).

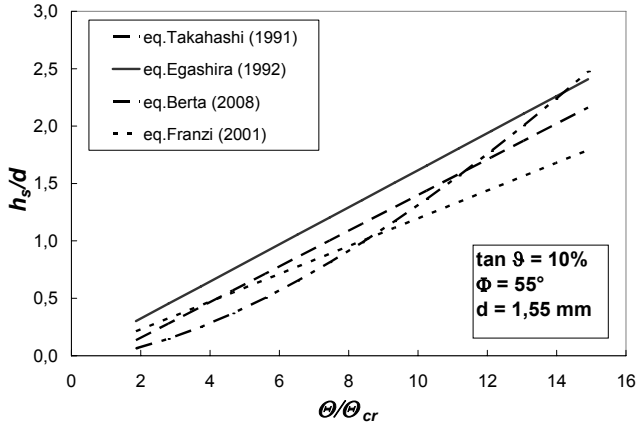

Fig. 2. Non-dimensional moving layer depth, h_s/d, against Θ/Θ_{cr}, estimated with different expressions developed for steady flows. Values of slope, friction angle and diameter used for the estimation are shown in the figure.

and Bowles, 2006), we have reproduced a rapidly changing unsteady flow through the overtopping of a granular steep slope. To make our model comparable with the ones developed for open channels, only data relevant to the mono-dimensional erosion stage have been used for the calibration. Consequently, our model can be applied both to open channels and to embankments/dams, provided that the flows can be modelled as mono-dimensional and that the slopes and shear stress levels fall within the considered ranges.

2 Evaluation of moving layer depth in unsteady flow

It is observed that, during an erosive process, the moving layer depth, h_s (see Fig. 1), increases from zero (if the incoming stream is clear water) to a maximum value, when the transport capacity is completely satisfied (Egashira and Ashida, 1992). Many formulas for h_s have been developed for uniform flow condition, or "equilibrium condition", where the transport capacity is satisfied. For example, in Fig. 2 are represented Egashira and Ashida (1992), Takahashi (1991), Franzi (2001) and Berta (2008) expressions for the non-dimensional moving layer, h_s/d (d is the representative diameter). The curves in Fig. 2 show the trend of increasing h_s with Θ/Θ_{cr} (where Θ_{cr} is the critical Shields parameter), and describes only the equilibrium value of h_s, so this cannot describe the evolution of the moving layer. Hence, our purpose is to describe the evolution of the moving layer for generic unsteady conditions.

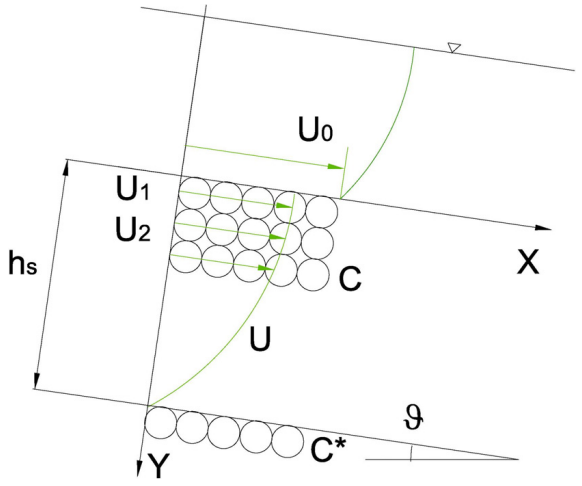

Fig. 3. Sketch of the sediment transport scheme.

We adopt a phenomenological scheme that was first proposed by Du Boys (Wan and Wang, 1994), then resumed by Chien and Wan (1999), Bianco and Franzi (1999), and Franzi (2001). Even though developed for steady conditions, this approach here is supposed to be valid also in unsteady conditions, by assuming all the variables varying in space and time. Our scheme considers an infinitely long bed of incoherent particles, with slope ϑ. The motion of each layer is assumed to be mono-dimensional and is thought to be due to two effects: the component of weight force parallel to the flow direction (x, see Fig. 3) and the drag of the flow, and the resistance to motion is due instead to the friction acting between the particles in the considered layer and those below it. Equilibrium equation for the x direction in uniform conditions can be written as follows:

$$\frac{\rho_w}{2}(u_0-u_1)^2\frac{\Pi\alpha^2 d^2}{4}+(\rho_s-\rho_w)\frac{\Pi}{6}\alpha^3 d^3\sin\vartheta = K_1 g(\rho_s-\rho_w)\frac{\Pi}{6}\alpha^3 d^3\cos\vartheta \quad (1)$$

where u_0 is the flow velocity (defined in a time interval smaller than the time scale of the unsteadiness) over the first grain layer; u_1 is the velocity of the first layer; K_1 is a dimensionless coefficient which takes into account the frictional effects due to interaction between water and sediment; g is the acceleration due to gravity, ρ_s and ρ_w are sediment and water density, respectively; α is a coefficient related to the particles

distance (which can be less or more than diameter d) and supposed to assume the form:

$$\alpha = \beta\sqrt{\frac{\tau_0}{\tau_c}}, \tag{2}$$

where β, unknown, is a calibration parameter, τ_0 the bottom shear stress and τ_c its critical value. After simplifications, the equation system which describes each layer motion is:

$$\begin{cases} (u_0-u_1)^2 = \frac{4}{3}\left(\frac{\rho_s}{\rho_w}-1\right)\alpha g d\,(K_1\cos\vartheta-\sin\vartheta) \\ (u_1-u_2)^2 = \frac{4}{3}\left(\frac{\rho_s}{\rho_w}-1\right)\alpha g d\,(2K_2\cos\vartheta-\sin\vartheta),\ldots, \\ (u_{n-1}-u_n)^2 = \frac{4}{3}\left(\frac{\rho_s}{\rho_w}-1\right)\alpha g d\,(nK_2\cos\vartheta-\sin\vartheta) \end{cases} \tag{3}$$

where coefficient K_2 takes into account the effects of the superior moving layers and the resistance effect of the lower ones. Following Takahashi (1991), K_2 is assumed:

$$K_2 = \left(\frac{c^*}{C_v}\right)^{\frac{1}{3}}\tan\Phi, \tag{4}$$

where C_v is the average concentration of the water sediment flow and c_* is the mean dry volumetric concentration of the bottom. Dividing each equation by $(\partial y)^2 \cong (\alpha d)^2$, the equation system can be rewritten in a differential form:

$$\left(\frac{\partial u}{\partial y}\right)^2 = \frac{4}{3}(K_2 y\cos\vartheta-\alpha d\sin\vartheta)\,g\left(\frac{\rho_s}{\rho_w}-1\right)\frac{1}{(\alpha d)^2} \tag{5}$$

Equation (5) is integrated in space (boundary condition: $u(0)=u_1$), and divided by the friction velocity, $u*$. The moving layer depth, h_s, is established by imposing $u(h_s)=0$.

$$\frac{h_s}{d} = \left(\frac{3}{2}\tilde{N}\beta\right)^{\frac{2}{3}}\left(\frac{\Theta}{K_2^*}\right)^{\frac{1}{3}}\left(\sqrt{\frac{\Theta}{\Theta_c}}-1\right)^{\frac{2}{3}} \tag{6}$$

In Equation (6), Θ_c is the critical Shields parameter (corrected for slope); Θ is the Shields parameter and is estimated for unsteady flows with the energy slope, S_e, instead of the bottom slope (Graf and Song, 1995):

$$\Theta = \frac{\tau_0}{(\gamma_s-\gamma)d} = \frac{R\,S_e}{\left(\frac{\rho_s}{\rho}-1\right)d}; \tag{7}$$

$\tilde{N}$ is the approximation of expression u_0/u_* for critical incipient motion condition; and

$$K_2^* = 4/3(K_2\cos\vartheta-\sin\vartheta). \tag{8}$$

The function $\left(\frac{3}{2}\tilde{N}\beta\right)^{2/3}$ is supposed to depend on hydrodynamical conditions, Θ_c/Θ, and on sediment diameter, d. Our model is consequently written as:

$$\frac{h_s}{d} = F\left(\frac{\Theta_c}{\Theta}, d\right)\left(\frac{\Theta}{K_2^*}\right)^{1/3}\left(\sqrt{\frac{\Theta}{\Theta_c}}-1\right)^{2/3}. \tag{9}$$

The use of Eq. (9) requires the calibration of function F, obtained through the dataset provided by laboratory tests, as will be explained in the following sections.

3 Experimental Setup

3.1 Hydraulic setup

Laboratory experiments were conducted in a 20 m long, 0.395 m wide straight flume with plexiglass walls and a slope equal to if=0.00715. A 0.395 m wide trapezoidal wooden template, composed of several modules, was located at the end of the flume (Fig. 4). The embankment was made erodible over a width of 0.095 m next to the left side of the flume by substituting one of the fixed modules with granular material. The sediment was thoroughly mixed by hand and shaped like a wooden dam (Fig. 4). A 0.03 m thick and 0.70 m long drain was placed under the embankment to prevent failure during the filling of the flume. The water level in the flume was raised to the level of the embankment crest (about 0.13 m); when water started to flow over the structure, the canal was no longer fed and the breaching process spontaneously evolved. The canal freely emptied at a rate that was dependent on the erosion development. A metal plate septum, placed behind the embankment, narrowed the width of the flume to 0.095 m and ensured a regular and parallel flow. Water discharge, Q_w, which flew over the embankment, was estimated through the variations in time of water volume in the flume, detected by a level probe. Adopting the experimental techniques used by Visser (1998) and Coleman et al. (2002), the water levels were measured (at 10 Hz) by the probe which was positioned upstream to the structure. As the overtopping discharge progressively eroded the embankment, a hopper at the end of the flume collected water and the sediment output. A sediment trap was placed under the hopper: the trap base, made of a mesh filter, was linked to a loading cell which recorded the dynamic force of the water-sediments (frequency 10 Hz). Data processing allowed the sediment discharge, Q_s, to be estimated. The erosion process was videotaped from downstream with a digital video camera and photographed with a digital camera (respectively VC1 and DC1 in Fig. 3) placed on one side of the flume. The profiles and local slopes of the free stream surface and of the embankment were recognized from each frame. Moving layer measures, h_s, were acquired along inner sections over the slopes.

3.2 Sediment properties

In order to analyse the influence of the sediment mean diameter on the moving layer depth, three different sediments (named A, B and C) were used to build erodible embankments. Some of their key properties are shown in Table 1.

The influence of the sediment compaction on the sediment friction angle and, hence, on the erosion rate (represented by the moving layer depth), was only qualitatively observed by Morris et al. (2007). The same influence was studied here by creating different compaction zones in the embankment. In fact, according to Bolton's theory (Bolton, 1998), sediment

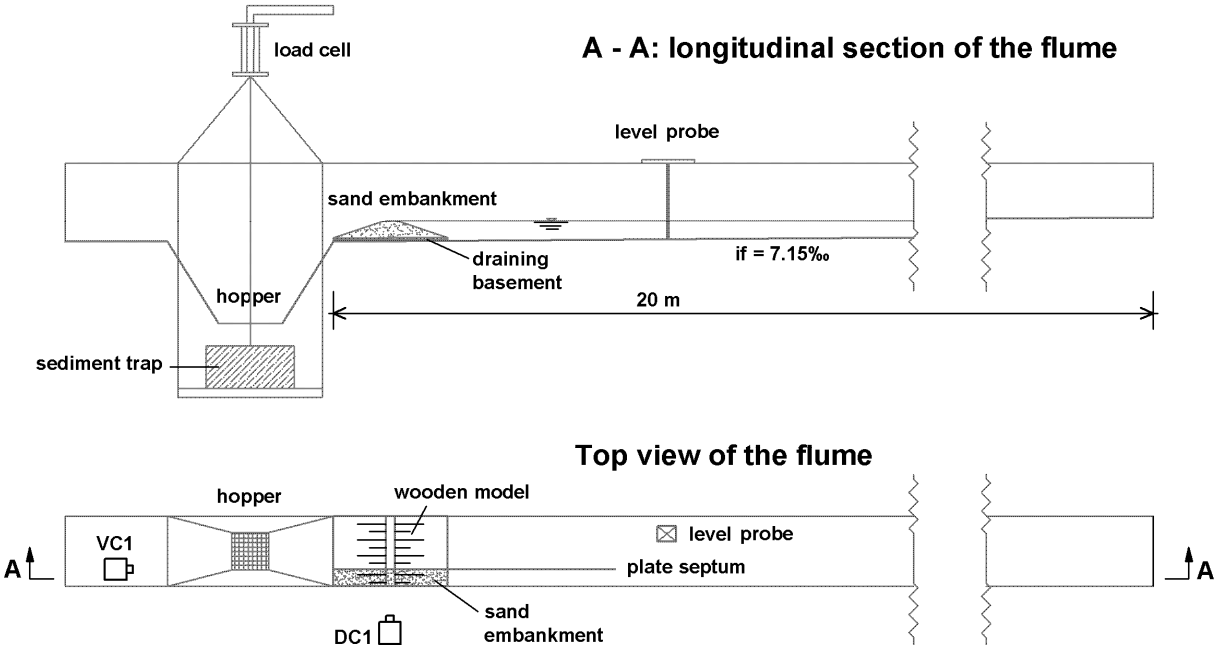

Fig. 4. Sketch of the flume in the experiment. Water flows from right to left.

Table 1. Properties of sediments and embankments: for the three sediments (indicated as A, B, C) are shown the different granulometry, the mean diameter, d_{50}, and the specific gravity G_s. For the different embankments are collected the mean dry volumetric concentrations, c_*.

Sediment and reference test	A (test 31)	B (test 28)	C (test 26)
Granulometry (mm)	0.1-0.71	1.41–1.68	50%(1.41–1.68) 50%(0.35–0.5)
d_{50} (mm)	0.86	1.55	0.99
G_s	2.649	2.663	2.656
c^*	0.565	0.620	0.631

Table 2. Constant volume Φ_{cv} (measured using a tilting table covered by fixed grains of the same size) and peak friction angle Φ_p (measured for specimens with relative density DR=25).

Sediment	A	B	C
Φ_{cv} (°)	37.3	39.1	38.7
Φ_p (°)	53.4	55.9	55.0

relative density, DR, affects friction angle, Φ. It should be pointed out that what is commonly identified as friction angle is in fact the peak friction angle, Φ_p, which assumes a lower value for sediment in a loose state (Φ_{cv}: constant volume friction angle) and increases, due to a dilatancy phenomenon, with the relative density, DR (Bolton, 1998). According to Bolton's theory, we have experimentally enhanced the friction angle through a particular building technique. As the embankment was built layer by layer, the most internal region was more compacted than the external one, while the sediment in the upper layer could be considered in a loose state. During our tests, water overflowed the embankment and the erosion, in time, affected the layers with increased compactness: for the sake of simplicity, we have considered the structure to be divided into five zones with homogeneous compaction (and, hence, relative density DR) (Fig. 5). Tests on specimens for each sediment composition were performed in order to assign reliable peak and constant volume friction angle value to each embankment zone (Table 2). An average friction angle, representative of the three sediments, was assigned to each compaction zone: the maximum peak friction value (55°) assigned to the bottom layer, was decreased to the critical value (39°) for the upper one (Table 3).

Table 3. Description and average peak friction angle Φ_p (representative of the three materials A, B, C) for the embankment layers, identified through the downstream embankment slopes $\tan\vartheta$.

Layers	Range of slopes	Average Φ_p
surface	0.33	39°
1	$0.33 < \tan\vartheta < 0.25$	43°
2	$0.25 \leq \tan\vartheta < 0.17$	47°
3	$0.17 \leq \tan\vartheta < 0.09$	51°
4	$0.09 \leq \tan\vartheta \leq 0$	55°

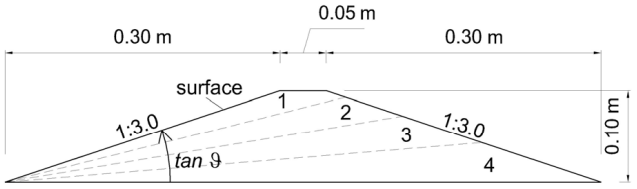

Fig. 5. Cross-section of the embankment with the hypothesis of five homogenous compactness zones (identified as surface, 1, 2…4). The erosion, in time, affected layers with increasing compactness: at first, the upper layer (surface and nr. 1) and afterwards the lower layers (nr. 2–3). Flume water is on the right side of the section.

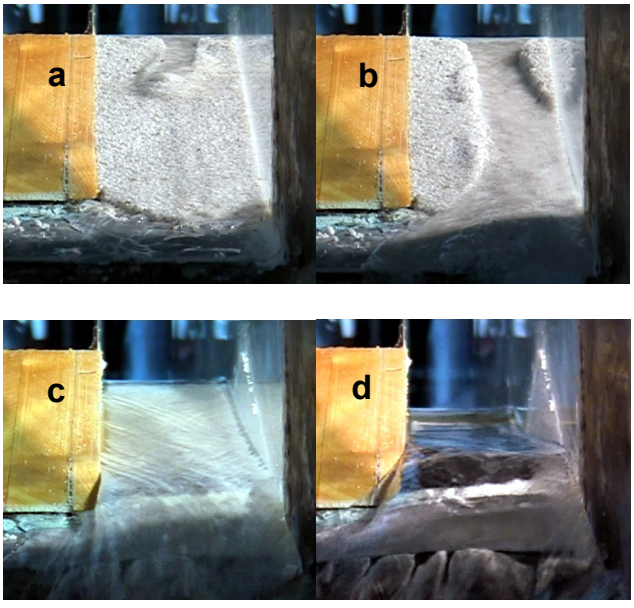

Fig. 6. Downstream view of the embankment erosion. **(a)** Stage 1: water reaches the embankment crest, particles are easily moved and a little debris flow originate. **(b)** Stage 2: erosion of the slopes, started in small rills, continues within small channels progressively widening to the whole width. Increasing scour lead, increasing water discharge so debris flow evolves into immature debris flow. **(c)** Stage 3: water sediment stream, occupying all the embankment width, is approximately mono-dimensional: during this phase a great amount of data were collected by pictures taken through the transparent wall of the canal. Immature debris flow evolved towards ordinary bed load. **(d)** Stage 4: when the structure was completely removed, the water discharge began to decrease and the flume emptied.

4 Results

The erosion of the embankment reproduced a continuous evolution of streams from debris flows to ordinary bed loads. A distinction of the different stages of erosion is useful to underline the occurrence of a stage (the third) in which the water sediment stream was approximately mono-dimensional. The data acquired during this stage were considered comparable to open channel data, and were used to calibrate Eq. (9).

4.1 Erosion stages of embankment

As the overflowing began, four stages were observed, with the consequent erosion.

In the first stage (Fig. 6a), the opening of one or more breaches was recognized. Crest particles, in a loose state, were easily moved by the initial overflowing discharge: as a result, a sliding of sediment particles occurred and a small debris flow started. In the second stage (Fig. 6b), the erosion of the slope continued in small channels and progressively expanded laterally to cover the whole slope width. The increased scour led to an increased water discharge, with a significant unsteadiness. The third stage (Fig. 6c) began when the stream occupied the whole slope width and the erosive phenomenon affected only the embankment bed, and progressively reduced its slope. From the beginning of this phase until the complete embankment erosion, the stream appeared dominated by the longitudinal velocity component, in a process that could be regarded as well approximated by a one-dimensional flow model. In the fourth and last stage (Fig. 6d), the flume emptied: this stage began at the complete erosion of the structure, when the water was able to occupy the whole transverse section.

4.2 Water, sediment discharges and sediment concentration

The overflowing water discharge, Q_w, is computed by subtracting the seepage discharge from the total discharge flowing out of the flume, dV/dt (variation in time t of the water volume V in the flume). Figure 7 reports the evolution in time of the water discharge, $Q_w(s_L,t)$, downstream the last embankment section, s_L (Fig. 8). The sediment discharge, Q_s, represents the erosion rate of dry material eroded along two subsequent embankment profiles in the time step Δt, referring to the embankment toe section s_L: it is also identified as $Q_s(s_L,t)$. Sediment discharge was obtained by both analysing load cell data, $Q_s(s_L,t)_{cell}$, (distinguishing the force due to solid particles – supposed loose and saturated – from the dynamic action of the water discharge), and pictures data, $Q_s(s_L,t)_{picture}$ (Fig. 7). The sediment concentration C_v was estimated as the ratio between the sediment discharge, Q_s, and the overall mixture discharge of the flow out of the embankment (section s_L). Apart from the sediment and water discharges (Q_s and Q_w, respectively), the contribution of the saturation water contained in the voids of the eroded sediment, $Q_{w,voids}$, was also considered for mixture

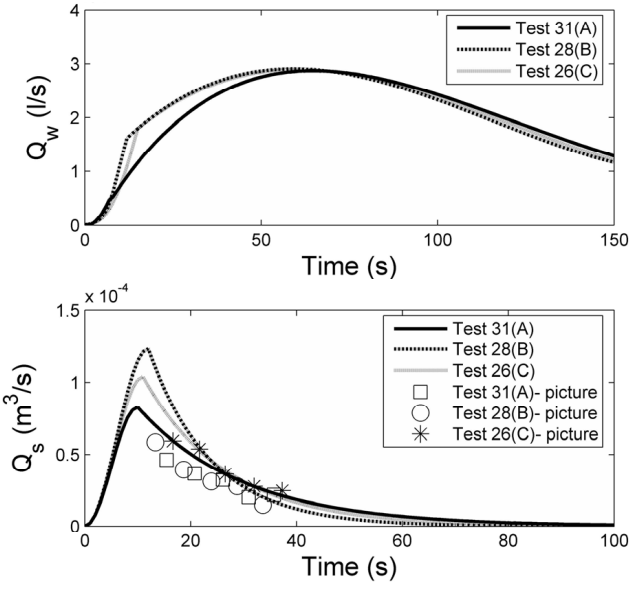

Fig. 7. Water discharge, Q_w, (measured by level and probe) and sediment discharge, Q_s, (measured by load cell and deduced by pictures), for three different embankment compositions (A, B, C).

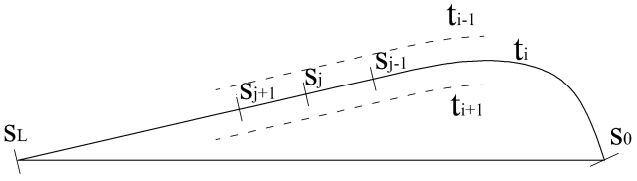

Fig. 8. Evolution in time of embankment profiles. For a generic profile, the first section, s_0, the last one, s_L, and some intermediate sections, s_j, are shown.

discharge

$$C_v = \frac{Q_s}{Q_s + Q_w + Q_{w,voids}}, \tag{10}$$

$$Q_{w,voids} = Q_s \frac{(1-c*)}{c_*} \tag{11}$$

where $(1-c_*)$ was the mean embankment porosity (Table 1). The experimental values of the sediment concentration $C_v(s_L,t)$ are plotted in Fig. 9, showing how the visual observations of the pictures were consistent with the measurements obtained with the load cell. C_v measures on the last section were used to calibrate the following expression for the sediment concentration in unsteady flows (Berta et al., 2008):

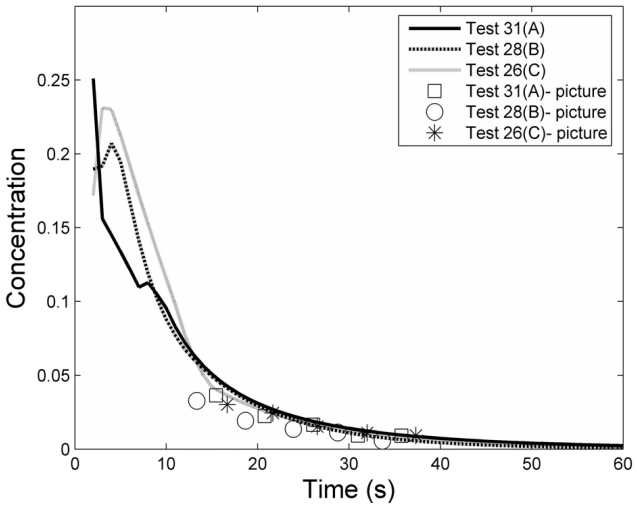

Fig. 9. Mean sediment concentration in time (measures from load cell and probe and from pictures analysis), related to the last embankment section s_L.

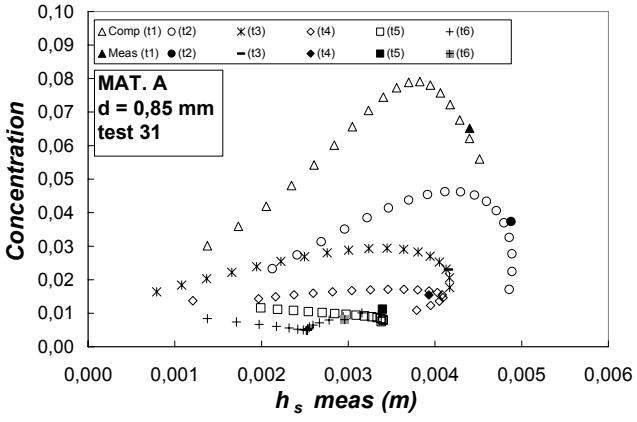

Fig. 10. Third stage. Mean sediment concentration in time (C_v) against moving layer (measured) depth (h_s). Among C_v measures on the last embankment section, s_L, are reported the C_v computed by Eq. (12) for all inner sections.

$$C_v(s,t) = \frac{12.5\left(\frac{\Theta_c(s,t)}{\Theta(s,t)}\right)^{0.45}}{(\tan\Phi(s,t))^{1.6}} \frac{\frac{1}{\Delta}\left[1-\frac{\Theta_c(s,t)}{\Theta(s,t)}\right](\tan\vartheta(s,t))^{1.9}}{1+\frac{1}{\Delta}\left[1-\frac{\Theta_c(s,t)}{\Theta(s,t)}\right](\tan\vartheta(s,t))^{1.9}} \tag{12}$$

where $\Delta = (\rho_s/\rho) - 1$. The data measured during the third stage along embankment profiles were introduced into Eq. (12) to obtain a reliable estimation of sediment concentration also for the inner sections (Fig. 10).

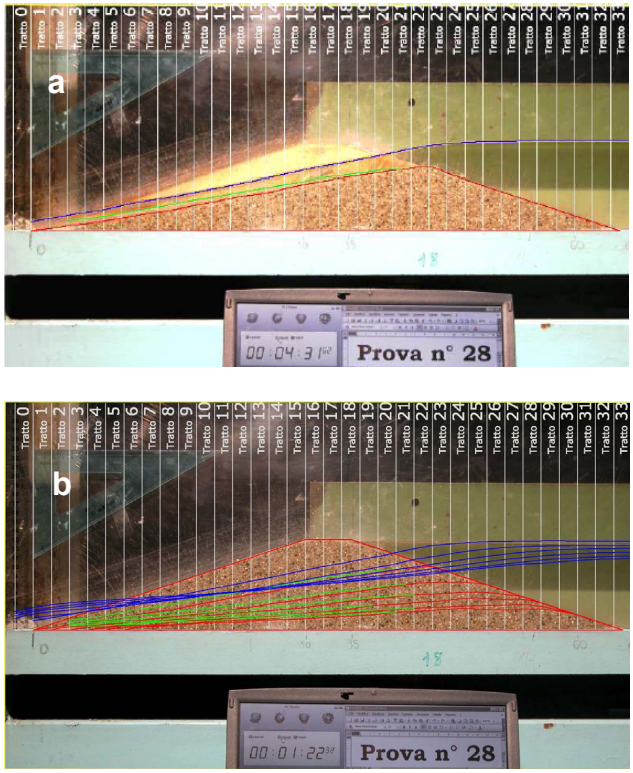

Fig. 11. Third stage – embankment lateral picture. **(a)** Example of picture analysis during the third stage: water profile (blue), bed profile (red) and moving layer profile (green) are drawn on the picture. **(b)** Example of evolution in time of bed, flow and moving layer profiles.

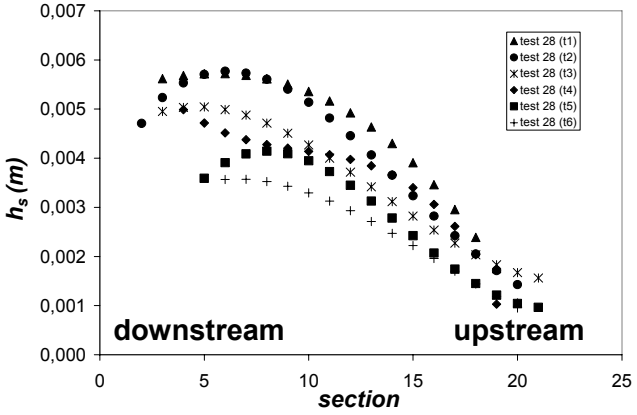

Fig. 12. Example of evolution in time (picture time t_1, t_2,...) of moving layer thickness, h_s, increasing from upstream to downstream. For a fixed section, h_s decreases in time, following the sediment discharge trend (see Fig. 7).

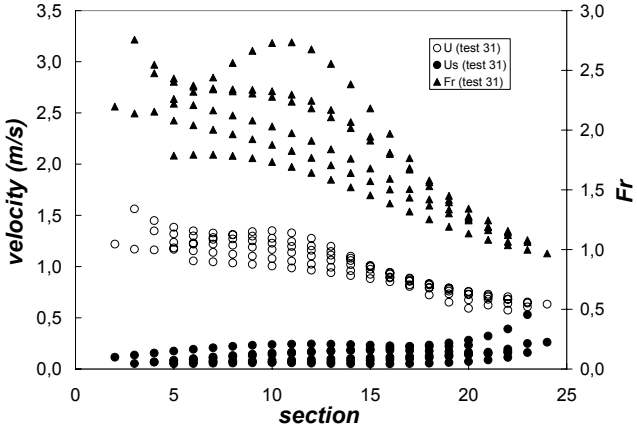

Fig. 13. Example (test 31) of evolution along embankment sections (s_j) of water and sediment velocities (u_w and u_s, respectively) and Froude numbers (Fr).

4.3 Moving layer depth and flow velocity during the third stage

Pictures taken from the lateral wall during the third stage were used to measure, along a fixed grid, the total water depth, h_t, the moving layer depth, h_s, the water depth, h_w, the local bed slope, ϑ, and the free surface slope, i (Fig. 11a, b). In Fig. 12, it can be noticed, for a fixed instant, how h_s increases from upstream to downstream, as the flow progressively enhances its concentration trying to satisfy its transport capacity.

Data acquired during this phase were also used to compute the local mean velocities: in Fig. 13 we notice the littleness of sediment velocity u_s with respect to flow velocity u_w. In the same figure, the Froude numbers are also represented, which varied from 0.77 to 3.41. The flows results were fully turbulent, in fact, the particle Reynolds number varied from 80 to 270, and the Reynolds number varied from 4.5×10^4 to 1.5×10^5, with a relative roughness of 0.030 to 0.004.

4.4 Data analysis

Morphological processes in unsteady conditions tend to become equilibrium shapes, correlated to the instantaneous water discharge (Seminara, 1998). We have verified this assessment by comparing non-dimensional moving layer measures $h_s/d(s_j,t_i)$ to equilibrium curves computed with Egashira equation (Egashira and Ashida, 1992) (plotted for representative mean slopes and friction angles). For each instant, t_i, $h_s/d(s_j,t_i)$ measures increase along the embankment profile, while $\Theta_c/\Theta(s_j,t_i)$ decrease: the arrows in Fig. 14a, b, and c clearly indicate the tendency toward equilibrium of the experimental series. The equilibrium achievement is, on the contrary, not obviously verifiable: in fact, it depends on the equilibrium expression adopted and on the estimation of parameters like friction angles. Therefore, h_s/d series seem to

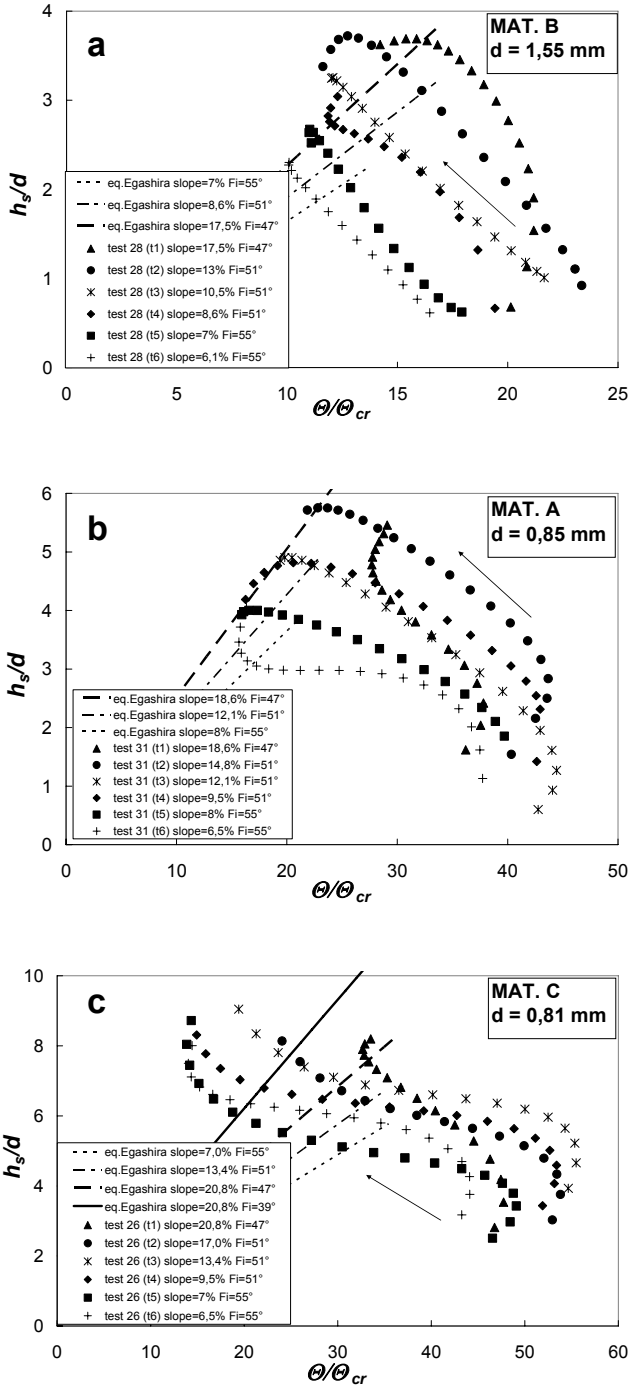

Fig. 14. Comparison between measures of moving layer relative depth (h_s/d) vs. Θ/Θ_c and Egashira (1992) equilibrium curves. Since Egashira equation does not show significant variations with slope (for fixed $\Theta/\Theta_c(s_j,t_i)$), it is shown here, for simplicity only, three reference equilibrium curves, computed for the friction angles involved (Φ=47°,51°, 55°) and for three representative slopes. From experimental data, it seems that equilibrium is reached but lost again around the last embankment sections: in **(c)** h_s/d values are even over Egashira equation computed with the minimum friction angle (39°).

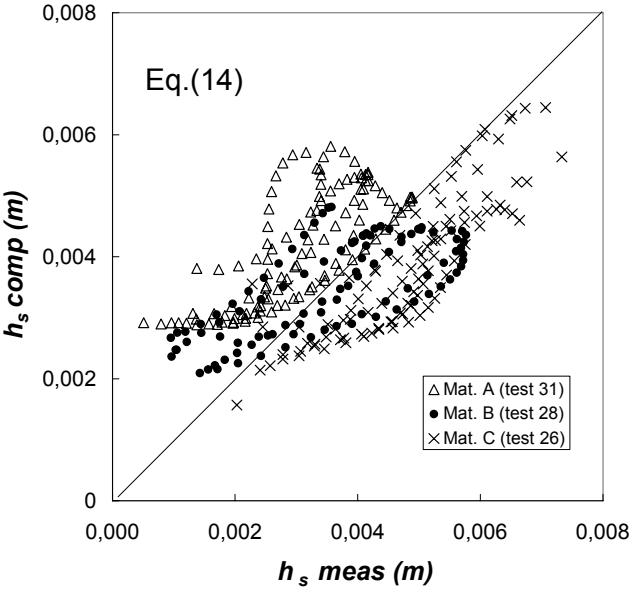

Fig. 15. Measured and computed (Eq. 14) values of moving layer depth.

reach equilibrium and then to lose it again (Fig. 14c) around the embankment toe. Moreover, on the last embankment section, the embankment is thin, and a few effective compactions could have led to friction angles being smaller than supposed. This could explain how experimental data for the last sections tended to the equilibrium curve with friction angles smaller than supposed.

4.5 Calibration

The measurements collected during the third stage of erosion, related to approximately mono-dimensional streams, were comparable with the open channel data and, hence, were used to calibrate Eq. (9). Values of $F(s_j,t_i)$, related to sections s_j at instants t_i, are computed by introducing into Eq. (9) measures of $h_s(s_j,t_i)$, $h_t(s_j,t_i)$, $\tan\Phi(s_j,t_i)$, $\Theta_c/\Theta(s_j,t_i)$ and estimations of $C(s_j,t_i)$ in non-equilibrium conditions (Eq. 12). All $F(s_j,t_i)$ values are acceptably interpolated by the function:

$$F(s,t) = 400\left(\frac{\Theta_c(s,t)}{\Theta(s,t)}\right)^{(40d^{0.46})} \tag{13}$$

The simplified calibrated model is:

$$\frac{h_s}{d}(s,t) = 107\left(\frac{\Theta_c}{\Theta}(s,t)\right)^{(204d^{0.79})}$$

$$\left\{\frac{4}{3}\cos\vartheta(s,t)\left[\left(\frac{c^*}{C_v(s,t)}\right)^{1/3}\tan\Phi(s,t)-\tan\vartheta(s,t)\right]\right\}^{-1/3}, \tag{14}$$

with C_v computed with Eq. (12). The accuracy of the calibration is appreciable in Fig. 15. To conclude, our

model, Eq. (14), can be used, for $10.1 \leq \Theta / \Theta_c \leq 55.5$ and $0.03 \leq \tan\vartheta \leq 0.20$, to estimate the moving layer depth of an unsteady non-uniform flow.

5 Conclusions

Erosional processes in natural flows are typically unsteady. When the time dependence is strict, the instantaneous adaptation between solid and liquid phases is not reliable, and the use of equilibrium expressions derived for steady flows become incorrect. This paper has investigated the sediment transport for unsteady conditions through the "moving layer", by proposing a new expression for the moving layer depth and calibrating it with experimental data. A succession of unsteady flows have been reproduced in tests performed in a laboratory flume on a steep, uniform and mixed sediment slope. The experiments have shown moving layer depths increasing from upstream to downstream, so confirming the tendency of the bottom to reach the morphodynamical equilibrium for the varying liquid discharge (Seminara, 1998). This study has highlighted how difficult it is to know for certain the equilibrium achievement, not only for the choice of the equilibrium expression, but also for the estimation of the parameters involved in it (e.g. friction angle). The expression developed for unsteady flows is valid in the $10.1 \leq \Theta / \Theta_c \leq 55.5$ and $0.03 \leq \tan\vartheta \leq 0.20$ experimental field. This novel formulation is easy to apply within mathematical models and gives a reliable estimation of the moving layer depths during unsteady conditions, where the transport capacity could not be satisfied and where the commonly used expressions for uniform conditions fail. Our model can be applied both to open channels and to embankments/dams, provided that the flow can be modelled as mono-dimensional, and that the slopes and applied shear stress levels fall within the proposed ranges.

Acknowledgements. The authors are grateful to Renato Lancellotta, Luca Ridolfi, Luca Franzi and Andrea Marion for their useful suggestions.

Edited by: L. Franzi
Reviewed by: B. Zanuttigh and A. Recking

References

Armanini, A. and Di Silvio, G.: A one-dimensional model for the transport of a sediment mixture in non-equilibrium condition, J. Hydraul. Res., 26(3), 275–292, 1988.

Berta, A. M.: Interaction between solid and liquid phases in unsteady granular flows. Theoretical and experimental study, Ph.D. thesis, Politecnico di Torino, Italy, 2008.

Berta, A. M., Bianco, G., and Franzi, L.: Sediment concentration of water sediment flows due to erosion of granular material over steep slopes, in: Proc. Int. Conf. on Fluid Hydraulics River Flow 2008, Cesme-Izmir, Turkey, 1725–1732, September 2008.

Bianco, G. and Franzi, L.: Mature and immature debris flows by solid load deduced from the study of acting stresses, in: Proc., First Int. Symp. on River, Coastal and Estauarine Morphodynamics, IAHR, Genova, Italy, 1999.

Bolton, M. D.: The strength and dilatancy of sands, Géotchnique, 1, 65–78, 1998.

Cao, Z., Pender, G., Wallis, S.m and Carling, P.: Computational dam-break hydraulics over erodible sediment bed, J. Hydraul. Eng.-ASCE, 130(7), 689–703, 2004.

Chien, N. and Wan, Z. (Eds.): Mechanics of Sediment Transport, ASCE, New York, 1999.

Coleman, S.E., Andrews, D.P., Webby, M.G.: Overtopping breaching of noncohesive homogeneous embankments, J. Hydraul. Eng.-ASCE, 128(8), 829–838, 2002.

Correira, L., Krishnappan, B. G., and Graf, W. H: Fully coupled unsteady mobile boundary flow model, J. Hydraul. Eng.-ASCE, 118(3), 476–494, 1992.

Di Silvio, G. and Gregoretti, C.: Gradually varied debris flow along a slope, in: Proc., Int. Conf. Debris-Flow Hazards Mitig., ASCE, San Francisco, USA, 767–776, 1997.

Egashira, S. and Ashida, K.: Unified view of the mechanics of debris flow and bed load, in: Advances in Micromechanics of Granular Materials, edited by: Shen, H. H., Satake, M., and Mehrabadi, M., Elsevier, Amsterdam, 391–400, 1992.

Egashira, S., Itoh, T., and Takeuchi, H.: Transition mechanism of debris flows over rigid bed to erodible bed, Phys. Chem. Earth, 26, 169–174, 2001.

Fraccarollo, L. and Capart, H: Riemann wave description of erosional dam break flows, J. Fluid Mech., 461(1), 183–228, 2002.

Franzi, L.: On the sediment transport layer width: a simplified approach, in: Proc., Int. Symp. on River, Coastal and Estauarine Morphodynamics, IAHR, Obihiro, Japan, 2001.

Graf, W. H. and Song, T.: Sediment transport in unsteady flow, in: Proc., XXVI Congress of IAHR, London, 480–485, 1995.

Morris, M. W., Hassan, M., and Vaskinn, K. A.: Breach formation: Field test and laboratory experiments, J. Hydraul. Res., 45, 9–17, 2007.

Papa, M., Egashira, S., and Itoh, T.: Critical conditions of bed sediment entrainment due to debris flow, Nat. Hazards Earth Syst. Sci., 4, 469–474, 2004, http://www.nat-hazards-earth-syst-sci.net/4/469/2004/.

Seminara, G.: Stability and Morphodynamics, Meccanica, 33, 59–99, 1998.

Takahashi, T. (Eds.): Debris flows, IAHR, Balkema, Rotterdam, 1991.

Visser, P. J.: Breach growth in sand-dikes, Ph.D. thesis, Delft Univ. of Technology, The Netherlands, 1998.

Wan, Z. and Wang, Z. (Eds.): Hyperconcentrated flow, Balkema, Rottedam, 1994.

Wang, Z. and Bowles, D. S.: Three-dimensional non-cohesive earthen dam breach model. Part I and II, Adv. Water Resour., 29(9), 1528–1545, 2006.